Optical response of nickel-based superalloy Inconel-718 for applications in additive manufacturing

Cite as: J. Appl. Phys. 127, 245111 (2020); https://doi.org/10.1063/5.0006006 Submitted: 27 February 2020 . Accepted: 07 June 2020 . Published Online: 25 June 2020

Erin B. Curry , Sanjubala Sahoo, Chloe Herrera, Ilya Sochnikov , S. Pamir Alpay , Rainer J. Hebert, Brian G. Willis, Jie Qi, and Jason N. Hancock







ARTICLES YOU MAY BE INTERESTED IN

Quantitative non-destructive single-frequency thermal-wave-radar imaging of case depths in hardened steels

Journal of Applied Physics 127, 245102 (2020); https://doi.org/10.1063/1.5139643

Topologically switchable behavior induced by an elastic instability in a phononic waveguide Journal of Applied Physics 127, 245109 (2020); https://doi.org/10.1063/5.0005331

Atomic layer deposition of environmentally benign $SnTiO_X$ as a potential ferroelectric material Journal of Vacuum Science & Technology A 34, 01A119 (2016); https://doi.org/10.1116/1.4935650









Optical response of nickel-based superalloy Inconel-718 for applications in additive manufacturing

Cite as: J. Appl. Phys. **127**, 245111 (2020); doi: 10.1063/5.0006006 Submitted: 27 February 2020 · Accepted: 7 June 2020 · Published Online: 25 June 2020







Erin B. Curry, ^{1,2,a)} Sanjubala Sahoo, Chloe Herrera, Ilya Sochnikov, ^{1,2} S. Pamir Alpay, Rainer J. Hebert, Sirian G. Willis, Jie Qi, and Jason N. Hancock, Die

AFFILIATIONS

- ¹Department of Physics, University of Connecticut, Storrs, Connecticut 06269, USA
- ²Institute for Materials Science, University of Connecticut, Storrs, Connecticut 06269, USA
- ³Department of Material Science and Engineering, University of Connecticut, Storrs, Connecticut 06269, USA
- Department of Chemical and Biomolecular Engineering, University of Connecticut, Storrs, Connecticut 06269, USA

ABSTRACT

We present a broadband infrared and optical study of the compositionally complex nickel-based superalloy Inconel-718, a common material used in additive manufacturing using the direct metal laser sintering (DMLS) technique. We find a broad, featureless spectral emissivity, which is consistent with dc transport measurements and contextualize the results against literature reports of disordered metals. We show that electronic structure calculations based on first-principles modeling can explain most of the spectral weight distribution and show that the peculiar infrared optical properties in this class of materials can present challenges in accurately reporting remote temperature sensing in DMLS.

Published under license by AIP Publishing. https://doi.org/10.1063/5.0006006

I. INTRODUCTION

The emerging additive manufacturing (AM) technique, direct metal laser sintering (DMLS), is a complex process of layer-by-layer fabrication of a three dimensional part. Through DMLS, metal powder is spread across a powder bed in layers as thin as $20 \,\mu m$. A high energy laser (>200 W) focuses onto the powder and scans the surface with a defined raster pattern. When the laser interacts with the powder, some of the energy is reflected and scattered into the surrounding environment and between powder grains. The remaining incident energy is absorbed, rapidly heating the powder above the melting temperature T_m to form a localized melt pool. As the laser passes, the temperature decreases due to radiative, convective, and conductive heat losses to the environment, the surrounding powder, and through the build plate below (Fig. 1). Eventually, the temperature decreases enough that the melt pool goes through the liquid-to-solid phase transition and solidifies. The temperature history through DMLS, specifically the liquid-to-solid phase transition time and the melt pool cooling rate, is the most important factor in the microstructure and strength of the final product.

The key component to evolving metal DMLS technology past the prototype phase and into mass production rests primarily in studying the melt pool heat transfer. As Most studies attempting to model DMLS assume only conductive heat transfer and ignore radiative cooling. As DMLS is a high temperature process, radiative cooling from the surface of the melt pool cannot be ignored. To quantify the radiative cooling, we study the spectral emissivity $e(\omega)$ of the metal alloy. This intrinsic optical property determines how much laser energy is absorbed, scattered, and radiated, processes vital to the energy budget in DMLS. This study focuses on a particular metal often used in AM, the nickel-based superalloy Inconel-718; however, the scientific approach can be applied to other alloys.

II. METHODS

For the experimental investigation of Inconel-718, a $17 \times 17 \times 1.5 \, \text{mm}^3$ parallelepiped was manufactured in an EOS M270 direct laser sintering system. The laser used to sinter the Inconel-718 powder into the solid sample is an IPG-Photonics 200 W single mode Yb continuous wavelength fiber laser at a

^{a)}Authors to whom correspondence should be addressed: erin.curry@uconn.edu and jason.hancock@uconn.edu

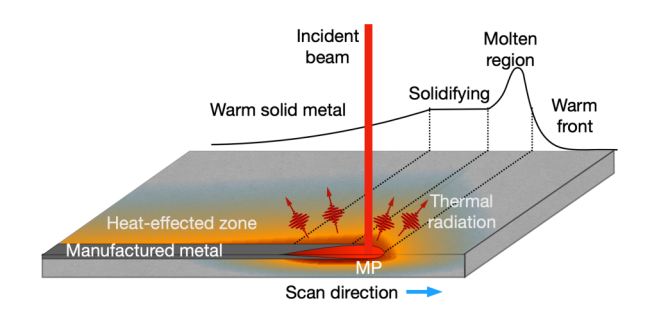


FIG. 1. An illustration of DMLS showing the energy transfer from the incident beam to the powder bed, where the melt pool (MP) forms and cools to create a manufactured metal. Powder in the surrounding regions, which is heated but not melted, is referred to as the heat-effected zone. The black solid curve represents the instantaneous temperature profile along a cut through the center of the melt pool and along the scan direction, indicating various regions of powder heating and melting, followed by solidifying and cooling the manufactured metal.

energy of $1.15 \, \text{eV}$ ($1.07 \, \mu \text{m}$). Following the manufacturing, the sample was set in clear epoxy, polished flat using alumina suspension with a finest grit size of $0.05 \, \mu \text{m}$, and finally buffed to produced a mirror-like surface free of visible scratches for the experimental goal of obtaining the complex dielectric constant $\varepsilon(\omega)$ of AM Inconel-718. To enable a meaningful extraction of the fundamental bulk optical quantities from our measurements, it is essential that the material represents a half space with a surface flat and smooth compared to the infrared wavelengths of interest. Below, we discuss the implications of realistic surface finish of additively manufactured Inconel-718 in the context of DMLS.

We employed two experimental techniques, ellipsometry and Fourier transform infrared (FTIR) spectroscopy, to access two sections of the energy spectrum at ambient temperature. Reflection ellipsometry was performed on a variable angle spectroscopic ellipsometry (VASE) rotating analyzer ellipsometer with an AutoRetarder waveplate to control the incident light polarization and captured both the real and imaginary parts of the dielectric constant directly through the ratio of s and p polarized reflected waves for the 1.25–3.5 eV $(0.35-1.0 \mu m)$ range. To access the lower energy range of $\varepsilon(\omega)$ and trend toward zero energy, we used the capabilities of a Bruker Optics IFS 66V/S FTIR spectrometer. Instead of direct $\varepsilon(\omega)$ measurement, FTIR spectroscopy utilizes a Michelson interferometer for reflectivity $R(\omega)$ information. Unlike ellipsometry, FTIR spectroscopy requires a reference reflected spectrum for which we used a thermally evaporated gold layer over half the polished Inconel-718. When not in use, the sample was stored in vacuum to reduce surface oxidation. The ratios between reflected spectra of Inconel and gold yielded Inconel reflectivity are on the spectral range of $0.15-1.25 \text{ eV } (1.0-8.3 \mu\text{m}).$

The FTIR reflectivity and ellipsometry are transformed using a Kramers–Kronig consistent analysis⁷ to derive the real and imaginary parts of the dielectric function, $\varepsilon_1(\omega)$ and $\varepsilon_2(\omega)$, respectively. Together, these quantities determine the complex index of refraction $n(\omega) = \sqrt{\varepsilon_1(\omega) + i\varepsilon_2(\omega)}$, which is related through Fresnel's equations to the reflectivity $R(\omega)$ and the spectral emissivity $e(\omega) = 1 - R(\omega)$.

In addition to measurements on additively manufactured Inconel-718, first-principles studies are performed to investigate the optical properties of Inconel-718 (Ni: 50.00-55.00, Cr: 17.00-21.00, Fe: 16.00-25.00 wt. %). We model this alloy by considering a Ni FCC supercell with 32 atoms where only the major alloy components are included: Ni (60 wt. %, 19 Ni atoms), Cr (25 wt. %, 8 Cr atoms), and Fe (15 wt. %, 5 Fe atoms). The minority components are assumed to play an insignificant role in derived properties and hence are neglected. The Cr and Fe atoms are substituted in the supercell by the appropriate number of Ni atoms (8 Cr atoms, 5 Fe atoms) in the FCC lattice site. Several random distributions of Cr and Fe atoms were considered to compute the total energies. The FCC supercell is constructed with an equilibrium lattice parameter value of pure Ni (a = 3.517 Å), which is in agreement with the previous literature as well as experimental values.8 The energetically stable configuration is determined by optimizing the configurations with several random distributions of Cr and Fe atoms of Ni₁₉Cr₈Fe₅.

The calculations are performed using the Vienna *ab initio* Simulation Package. The plane wave pseudopotentials are generated with the projector augmented wave (PAW) method. The geometry optimization is performed using the conjugate gradient algorithm. The forces on each atom are minimized using an energy convergence criteria of 10^{-6} eV. The integration over the Brillouin zone is performed with a $5 \times 5 \times 5$ k-mesh. The generalized gradient approximation (GGA) is used for the exchange and correlation functional and is parameterized by Perdew–Burke–Erzernhof. We compute the frequency-dependent ε_1 and ε_2 , which are determined using the density functional perturbation theory 12,13 or the linear response theory within the independent particle approximation and without including the effect of local fields. 13

III. RESULTS

Figure 2(b) shows the agreement between the FTIR measured $R(\omega)$ in the range of 0.15–1.25 eV (1.0–8.3 μ m) and the computed $R(\omega)$ determined from ellipsometry data from 1.25 to 3.5 eV (0.35–1.0 μ m), demonstrating the consistency of our approaches. A complementary study by del Campo *et al.* ¹⁴ focuses on spectral emissivity of metals including Inconel-718 with different solid surface treatments (wire-cut, sandblasted, and brushed) with surface roughness in the range of several micrometers. Samples in our current study are additively manufactured, polished, and much smoother than these treated surfaces, and the results seem to align with the trends in that work regarding the magnitude of the emissivity.

The reflectivity in Fig. 2(b) appears broad and featureless from the mid-infrared through the ultraviolet spectral ranges. Efforts to fit the optical response functions with a one-band Drude model are surprisingly effective over a broad spectral range. Our Drude fit includes the high-frequency dielectric constant $\varepsilon_{\infty}=2.81$, plasma frequency $\hbar\omega_p=13.2\,\mathrm{eV}$ (0.09 μ m), and the scattering rate $\Gamma=3.07\,\mathrm{eV}$ (0.40 μ m). The latter microscopic parameter, which quantifies dissipation and scattering of free carriers, is quite large, implying an extremely short relaxation time of order 1.3 fs.

A similarly short relaxation time was reported by Ray and Tauc in metallic glass $Fe_{80}B_{20}$, where, like Inconel-718, the

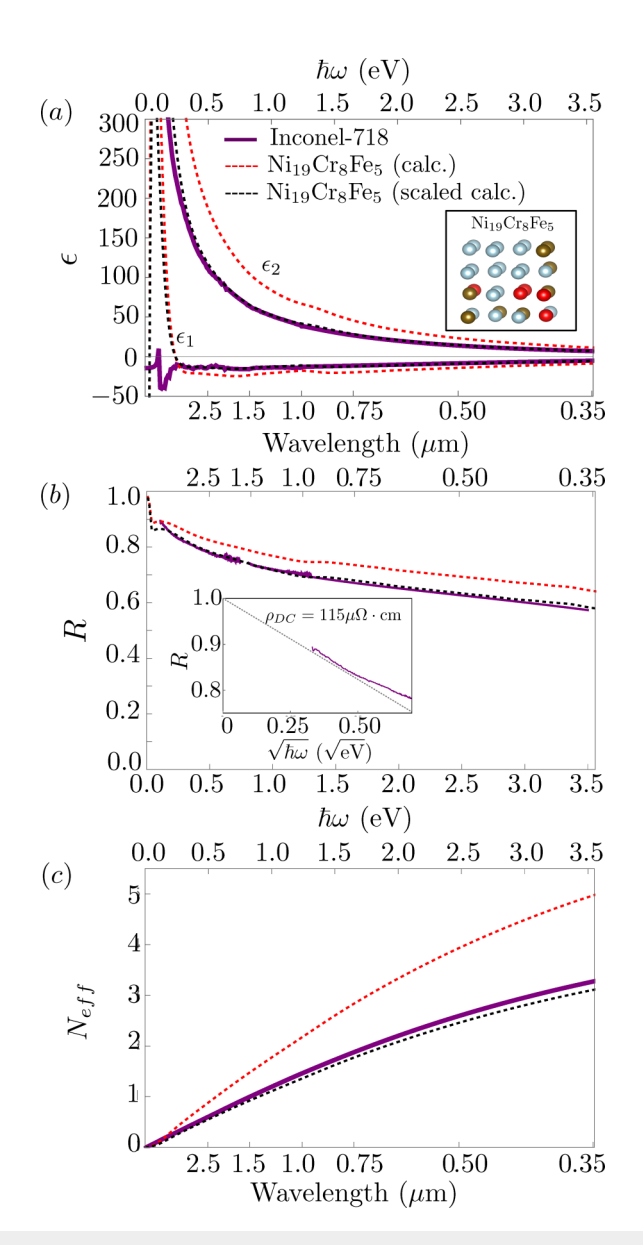


FIG. 2. (a) Dielectric functions ε_1 (dashed) and ε_2 (solid) of Inconel-718 at 300 K obtained through the Kramer–Kronig analysis of the reflectivity (purple), computed using density functional theory (DFT) (red), and a scaled computational result (black) showing excellent agreement with the experimental results. The inset shows the 32-atom Ni₁₉Cr₈Fe₅ supercell configuration used for calculations, with blue atoms portraying Ni, brown atoms Cr, and red atoms Fe. (b) Comparison of measured and calculated reflectivity at 300 K. The inset shows a dashed line of the measured ρ_{DC} for Inconel-718 along with our measured reflectivity as a function of the square root of the photon energy $\hbar\omega$. (c) Effective number of charges N_{eff} derived from the partial f-sum rule²³ applied to ε_2 .

reflectivity appears to follow a Drude model throughout the low energy regime. ¹⁵ This trend shows remarkable resemblance to the work of Hauser *et al.* on the optical response of amorphous $Au_{1-x}Si_x$ metallic glass alloys. The pure gold limit x=0 shows a

clear Drude component with a narrow width separable from the 5d to 6s and 6p interband transition onset near 2 eV (620 nm). Upon Si substitution of order x = 0.13, a dramatic broadening of the Drude width Γ is observed, while these interband transitions become broader and weaken. Above a concentration x > 0.30, the entire spectrum appears as a broad featureless continuum. 17

In addition to the broadband reflectivity of Inconel-718, we have also performed resistivity measurements using the van der Pauw method on the same sample and determined that the sheet resistance of our sample is $351\mu\Omega$. When combined with the measured thickness of 3.3 mm, we determine a bulk resistivity of $115\mu\Omega$ cm, fully consistent with prior reports. Within the Drude formalism, frequencies $\omega\ll\gamma$ define the Hagen–Rubens regime where the reflectivity $R(\omega)=1-4\sqrt{\pi\varepsilon_0c\omega\rho_{DC}}$ relates dc transport properties with the long-wavelength optical response. The dashed line in the inset of Fig. 2(b) shows this expectation based on the ρ_{DC} measurement along with our measured reflectivity as a function of the square root of the photon energy $\hbar\omega$. The excellent agreement implies that our measurements extend to sufficiently low frequency to capture the static behavior.

Some time ago, Mooij²⁰ reported a systematic trend among disordered alloys, which relates $d\rho_{DC}/dT$ to the magnitude of the resistivity ρ_{DC} . Briefly, as ρ_{DC} increases, $d\rho_{DC}/dT$ decreases with a sign change around $\rho_{DC}=150\,\mu\Omega$ cm. Our Inconel-718 dc resistivity is remarkably close to this Mooij threshold value, and indeed, most reports have a small 15% change in ρ from 400 to 1200 K. Additively manufactured Inconel-718 has a well-defined diffraction pattern dominated by the austenitic face-centered-cubic matrix γ phase, and the combination of secondary γ' , γ'' , and δ phases is vital to the precipitate strengthening effect and is likely an important contributor to disorder.

We expect that the precipitate matrix limits the validity of crystal momentum conservation in optical absorption processes and propose that a more local description of the electronic properties may be appropriate. We anticipate that a complete analysis of broadband excitations in the infrared should involve a large bandwidth, hybridized 4s and 3p states as well as crystal-field split d states with significant bandwidths of several eV. In order to assess the placement of their optical spectral weight, we present a set of density functional theory (DFT) calculations of the large 32-atom $Ni_{19}Cr_8Fe_5$ supercell shown in the inset of Fig. 2(a). Optical properties were then calculated from the electronic band structure and are presented in Fig. 2.

In Fig. 2(b), we compare the result of the calculation to the measured reflectivity over a broad range. The calculation and experiment appear to agree in the slope and smoothness throughout the infrared and visible ranges but with a notable and systematic overestimate of the computed reflectivity throughout this spectral range. Our zero-temperature DFT calculations do not include the effects of electron–phonon coupling, but such effects are not likely to enhance the spectral weight over experiments as observed. Systematic overestimates of optical spectral weight in DFT calculations are, however, well known and have been ascribed to fundamental limitations of DFT in handling Coulomb repulsion in correlated systems and can be used to estimate the degree of correlation in a particular system.²⁴ A detailed comparison of the spectral weight distribution in the optical response is enabled using the effective number of charges per

cell N_{eff} through direct integration of ε_2 , ²³ shown in Fig. 2(c). The calculated and measured N_{eff} are in excellent agreement after scaling the computed N_{eff} by 0.66, suggesting that Inconel is a moderately correlated electron system. ²⁴

The observed agreement between the spectral weight distribution throughout the mid-infrared is remarkable given the simplicity of the approach. Because radiative transfer is determined through thermal averaging of the emissivity, knowledge of the distribution of electronic weight and the gross features of the infrared response are adequate to address these properties. Such a connection may enable computational searches for new materials optimized for the manufacturing conditions of AM, which accounts for the optical contributions to radiative cooling. Such an approach would also fit recent efforts related to computational materials science as applied to manufacturing processes. More broadly, materials' data infrastructure may be employed for rapid screening of potential alloys given a particular set of processing conditions.

IV. DISCUSSION

The dielectric function over the infrared energy range gives vital information as to how incident electromagnetic waves interact with the material. In the context of AM, the high energy source is incident on the layer of metal powder on the build plate, and the interaction of the source causes the metal powder to absorb as well as scatter the electromagnetic source waves. DMLS is a dynamic and complex non-equilibrium process presenting experimental challenges to the assessment of heat transfer mechanisms behind cooling and solidification of the melt pool, and the relative importance of convection, conduction, and radiative transfer is a topic of some debate.²⁷ In conventional laser welding,²⁸ the thermal Marangoni effect or the mass flow responsive to a temperatureinduced surface tension gradient at the liquid-gas interface plays an active role in melt pool heat distributions at the local level. These circulatory flow patterns do not transfer heat outside of the liquidus region and, therefore, transfer heat only within and to the edges of the melt pool. Direct surface convection into the surrounding inert gas is estimated²⁹ with a convective coefficient of \sim 10 W/m² K, permitting an estimate of the cooling due to surface convection at $\pi (0.3 \,\mu\text{m})^2 10 \,\text{W/m}^2 \,\text{K} \sim 3 \,\text{nW}$, small in comparison with the incident power >200 W.

Direct heat conduction into the powder bed is likely important because within Fourier's Law, $q_{cond} \propto \nabla T$ and large thermal gradients are expected in the vicinity of the melt pool. Despite the presence of convection and conduction modes of heat transfer, the strong temperature dependence expected for radiative heat transfer (T^4 for a blackbody e=1) indicates that at the high superalloy melting temperatures $T_m > 1600 \, \mathrm{K}$, heat losses from the free surfaces of the molten region likely include a significant radiative component. ^{30,31} Promoppatum $et\ al.$ ³² compares a finite element model including radiative heat transfer to an analytical model, which treats conduction but ignores surface heat losses. Through comparison of the model that includes radiative cooling contributions to the one that is based solely on cooling through conduction, the report concludes that for the energy density above 0.4 J/mm, the two diverge significantly. ³² This suggests that radiative cooling is

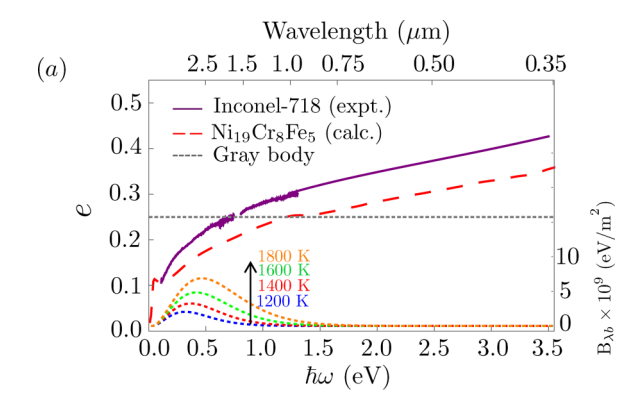
important in typical process parameter regimes. We explore here the consequences of our measurements on radiative cooling at elevated temperatures.

While the melt pool cools, energy is emitted in the form of electromagnetic waves spanning the energy spectrum and peaked at an energy determined by the temperature of the melt pool. For Inconel-718, the blackbody peak is around $0.4 \text{ eV} (3.10\,\mu\text{m})$ near the melting temperature [Fig. 3(a)]. The radiated intensity per unit wavelength per unit solid angle is $e(\lambda, \theta, T)B_{\lambda b}(\lambda, T)$, where $B_{\lambda b}(\lambda, T)$ is the spectral radiance given by Planck's law,

$$B_{\lambda b}(\lambda, T) = \frac{2hc^2}{\lambda^5 (e^{hc/k_B \lambda T} - 1)},\tag{1}$$

and the total power emitted per unit surface area A is

$$\frac{P}{A} = \int_{\lambda} \int_{\phi=0}^{2\pi} \int_{\theta=0}^{\pi/2} e(\lambda, \theta, T) B_{\lambda b}(\lambda, T) \cos \theta \sin \theta \, d\theta \, d\phi \, d\lambda. \tag{2}$$



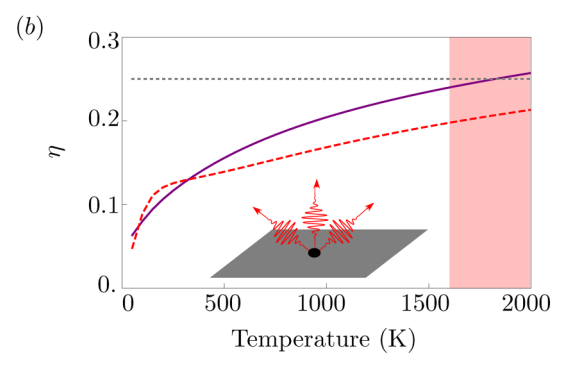


FIG. 3. (a) Emissivity comparison of Inconel-718 to the DFT calculated $Ni_{19}Cr_8Fe_5$ alloy and to the emissivity of a gray body emitter with e=0.25, suggestive of the variation in optical properties, which directly affect, respectively, radiative heating and cooling rates during the DMLS process. Dotted curves show spectral radiance given by Planck's law from below and above the melting point of Inconel-718. (b) The ratio of the total radiated power to that of an ideal blackbody is equal to the total hemispherical emissivity, shown here for measured Inconel-718, modeled $Ni_{19}Cr_8Fe_5$, and a gray body emitter. The red region indicates temperatures above the melting temperature $T_m=1600~\rm K$.

Here, $e(\lambda, \theta, T)$ is material dependent and is influenced by electronic structures and surface morphologies. In general, the spectral emissivity increases with rougher surface finishes as shown by the work of del Campo *et al.*¹⁴

For the limiting case e=1, Eq. (2) recovers the Stefan–Boltzmann law σT^4 , where σ is the Stefan–Boltzmann constant. Common practice assumes e is a constant, independent of both T and λ , which is referred to as the graybody approximation. In the case of Inconel 718, we have shown that e is a strong function of λ , consistent with other work. Broadband temperature-dependent emissivity has been reported over a limited range of temperatures $<600\,^{\circ}\mathrm{C}^{14}$ where minute <5% changes are observed near the blackbody peak, suggesting the dominant contribution to the radiated power is from $B_{\lambda b}(\lambda, T)$ and justifying in part an approximation to the spectral emissivity $e(\lambda, \theta, T) \approx e(\lambda, \theta)$ within the solid phase.

At the melting transition, Cagran et al.33 and Pottlacher et al. 34 both report an abrupt emissivity decrease at a single wavelength of 684.5 nm of 10% upon melting through $T_m = 1600 \,\mathrm{K}$ followed by a gradual linear increase with increasing temperature. In the liquid phase, however, the surface finish will be different from that of the solid phase, and therefore, the drop in emissivity at 684.5 nm is likely influenced by the surface changes upon melting. These emissivity trends are reported for a single wavelength, common practice due to the practical difficulties of experimentally determining broadband spectral emissivity at elevated temperatures. We cannot, therefore, assume that the shift is uniform across all wavelengths of interest. Furthermore, rigorous integral optical sum rules strongly constrain shifts in the optical response across wavelengths, and in many material systems, increases in some spectral regions are compensated by decreases in others, even crossing phase transitions characterized by strong electronic in electronic structures. ^{23,34} We have indicated the region above T_m in Fig. 3(b) where the temperature dependence of emissivity over all wavelengths is undetermined and for which the surface finish of Inconel-718 may shift the emissivity. Despite the possible bulk emissivity shift at $T > T_m$, at these extremely high temperatures, the spectral radiance contribution will dominate the T dependence of the thermal emissions.

As shown in Fig. 3(a), the emissivity of metal systems can vary quite a bit near the relevant wavelength region, depending on details of the electronic structure and associated optical transitions in the mid-infrared regime. Specifically, we expect that in the high temperature limit of DMLS, the simple T^4 law of radiative heat transfer will be significantly modified, providing a means to control cooling rates and, therefore, microstructural features of the manufactured metal part. To quantify the radiation emitted from the laser-sintered melt pool, we compare the computed emitted power per unit area with that of a perfect blackbody emitter $\eta = \frac{P/A}{\sigma T^4}$, which defines the total hemispherical emissivity. To determine the θ dependence of the emissivity, e in Eq. (2), we utilized the polarization-averaged reflectivity given by the Fresnel's equations.

Using the experimentally determined spectral emissivity of Inconel-718, Fig. 3(b) shows calculations of the total hemispherical emissivity alongside those of the DFT-modeled supercells. For reference, the horizontal dashed line shows η resulting from a graybody approximation with e = 0.25, and the strong deviation

illustrates the breakdown. Notably, this total hemispherical emissivity is a rather strong function of temperature in all cases, demonstrating that the common graybody approximation $e(\lambda) = \text{constant}$ is rather poor, and a strongly λ dependent $e(\lambda) \propto \sqrt{\rho_{DC}/\lambda}$ is more appropriate for Inconel 718.

In situ process monitoring of metal AM presents significant new technical challenges, as the spatial $(80\,\mu\mathrm{m})$ and temporal scales $(<1\,\mu\mathrm{s})$ are not well suited for most existing pyrometry approaches. As the state of the art in this area advances, thermal-emission based remote sensing technologies are likely to play a key role and will likely benefit from the availability of advanced optical materials as well as high speed detectors and electronics. As efforts to develop these approaches come to fruition, our results showing the strong wavelength dependence of Inconel-718 emissivity will benefit the associated temperature calibration relevant to *in situ* monitoring of metal AM.

V. CONCLUSION

We have presented a study of the broadband infrared properties of the nickel-based superalloy Inconel-718 using Kramers–Kronig transformations and find agreement with *ab initio* calculations based on a local picture of the electronic structure. The broad, featureless spectral reflectivity and emissivity are consistent with a Drude model and its long-wavelength Hagen–Rubens limit as well as the measured dc resistivity. We contextualize these results against prior literature reports in other disordered metals as well as applied physics work on Inconel-718 with different surface treatments and crossing the solid–liquid phase boundary. We find that the strong wavelength dependence of the optical properties of Inconel-718 limits the efficacy of certain common approximations related to DMLS pyrometry.

ACKNOWLEDGMENTS

The authors would like to recognize that the research reported in this publication was supported by Pratt and Whitney and their AM Center of Excellence at UConn. We also gratefully acknowledge the Air Force Research Laboratory, Materials and Manufacturing Directorate (AFRL/RXMS) for support via Contract No. FA8650-18-C-5700 and support from the National Science Foundation Grant No. NSF-DMR-1905862 and (NSF/CBET) Grant No. 1511138.

DATA AVAILABILITY

The data that support the findings of this study are available from the corresponding author upon reasonable request.

REFERENCES

¹N. Yu, "Process parameter optimization for direct metal laser sintering (DMLS)," Ph.D. thesis (National University of Singapore, 2005).

²D. Hu and R. Kovacevic, "Modelling and measuring the thermal behaviour of the molten pool in closed-loop controlled laser-based additive manufacturing," Proc. Inst. Mech. Eng. B: J. Eng. Manuf. 217, 441–452 (2003).

³M. H. Farshidianfar, A. Khajepour, and A. P. Gerlich, "Effect of real-time cooling rate on microstructure in laser additive manufacturing," J. Mater. Process. Technol. 231, 468–478 (2016).

- ⁴A. Gusarov, I. Yadroitsev, P. Bertrand, and I. Smurov, "Heat transfer modelling and stability analysis of selective laser melting," Appl. Surf. Sci. 254, 975-979
- ⁵E. Mirkoohi, J. Ning, P. Bocchini, O. Fergani, K.-N. Chiang, and S. Y. Liang, "Thermal modeling of temperature distribution in metal additive manufacturing considering effects of build layers, latent heat, and temperature-sensitivity of material properties," J. Manuf. Mater. Process. 2(3), 63 (2018).
- ⁶P. Michaleris, "Modeling metal deposition in heat transfer analyses of additive manufacturing processes," Finite Elem. Anal. Des. 86, 51-60 (2014).
- ⁷A. B. Kuzmenko, "Kramers-Kronig constrained variational analysis of optical spectra," Rev. Sci. Instrum. 76, 083108 (2005).
- ⁸H. P. Davey, "Precision measurements of the lattice constants of twelve common metals," Phys. Rev. 25, 753-761 (1925).
- ⁹G. Kresse and J. Furthmü, "Efficient iterative schemes for *ab initio* total-energy calculations using a plane-wave basis set," Phys. Rev. B 54, 11169 (1996).
- 10G. Kresse and D. Joubert, "From ultrasoft pseudopotentials to the projector augmented-wave method," Phys. Rev. B 59, 1758 (1999).
- 11 J. P. Perdew, K. Burke, and M. Ernzerhof, "Generalized gradient approximation made simple," Phys. Rev. Lett. 77, 3865 (1996).
- 12M. Gajdoš, K. Hummer, G. Kresse, J. Furthmüller, and F. Bechstedt, "Linear optical properties in the projector-augmented wave methodology," Phys. Rev. B 73, 045112 (2006).
- 13S. Baroni and R. Resta, "Ab initio calculation of the macroscopic dielectric constant in silicon," Phys. Rev. B 33, 7017-7021 (1986).
- 14L. del Campo, R. B. Pérez-Sáez, L. González-Fernández, X. Esquisabel, I. Fernández, P. González-Martín, and M. J. Tello, "Emissivity measurements on aeronautical alloys," J. Alloys Compd. **489**, 482–487 (2010).

 15S. Ray and J. Tauc, "Optical and magneto-optical properties of metallic glass
- Fe₈₀B₂₀," Solid State Commun. 34, 769-772 (1980).
- ¹⁶R. Lasser and N. V. Smith, "Interband optical transitions in gold in the photon energy range 2–25 eV," Solid State Commun. 37, 507–509 (1981).

 17 E. Hauser, R. J. Zirke, J. Tauc, J. J. Hauser, and S. R. Nagel, "Optical properties
- of amorphous metallic alloys," Phys. Rev. Lett. 40, 1733-1736 (1978).
- ¹⁸C. Herrera and I. Sochnikov, "Precision measurements of the AC field dependence of the superconducting transition in strontium titanate," J. Supercond. ovel Magn. 33, 201-203 (2019). arXiv:1904.03121.
- 19 G. Pottlacher, H. Hosaeus, E. Kaschnitz, and A. Seifter, "Thermophysical properties of solid and liquid Inconel 718 alloy," Scand. J. Metall. 31, 161-168
- ²⁰J. H. Mooij, "Electrical conduction in concentrated disordered transition metal alloys," Phys. Status Solidi A17, 521 (1973).

- ²¹S. R. Nagel, "Metallic glasses," in Advances in Chemical Physics (Wiley, 1982),
- pp. 227–276.

 22 X. Li, J. Shi, C. Wang, G. Cao, A. Russell, Z. Zhou, C. Li, and G. Chen, "Effect of heat treatment on microstructure evolution of Inconel 718 alloy fabricated by selective laser melting," J. Alloys Compd. 764, 639-649 (2018).
- ²³F. F. Wooten, *Optical Properties of Solids* (Academic Press, Inc., 1971), p. 260. ²⁴M. M. Qazilbash, J. J. Hamlin, R. E. Baumbach, L. Zhang, D. J. Singh, M. B. Maple, and D. N. Basov, "Electronic correlations in the iron pnictides," Nat. Phys. 5, 647-650 (2009).
- ²⁵S. Ewald, F. Kies, S. Hermsen, M. Voshage, C. Haase, and J. H. Schleifenbaum, "Rapid alloy development of extremely high-alloyed metals using powder blends in laser powder bed fusion," Materials 12, 1706 (2019).
- 26 The Minerals, Metals, and Materials Society (TMS), Advanced Computation and Data in Materials and Manufacturing: Core Knowledge Gaps and Opportunities (TMS, 2018).
- ²⁷R. J. Hebert, "Viewpoint: Metallurgical aspects of powder bed metal additive manufacturing," J. Mater. Sci. 51, 1165-1175 (2016).
- ²⁸S. Kou, Welding Metallurgy, 2nd ed. (John Wiley & Sons, Inc., 2003).
- 29 T. Zhang, H. Li, S. Liu, S. Shen, H. Xie, W. Shi, G. Zhang, B. Shen, L. Chen, B. Xiao, and M. Wei, "Evolution of molten pool during selective laser melting of Ti-6Al-4V," J. Phys. D: Appl. Phys. 52, 055302 (2019).
- 30 M. Chiumenti, X. Lin, M. Cervera, W. Lei, Y. Zheng, and W. Huang, "Numerical simulation and experimental calibration of additive manufacturing by blown powder technology. Part I: Thermal analysis," Rapid Prototyp. J. 23, 448-463 (2017).
- 31 J. Heigel, P. Michaleris, and E. Reutzel, "Thermo-mechanical model development and validation of directed energy deposition additive manufacturing of Ti-6Al-4V," Addit. Manuf. 5, 9-19 (2015).
- 32P. Promoppatum, S. C. Yao, P. C. Pistorius, and A. D. Rollett, "A comprehensive comparison of the analytical and numerical prediction of the thermal history and solidification microstructure of Inconel 718 products made by laser powder-bed fusion," Engineering 3, 685–694 (2017).

 33C. Cagran, H. Reschab, R. Tanzer, W. Schützenhöfer, A. Graf, and
- G. Pottlacher, "Normal spectral emissivity of the industrially used alloys NiCr20TiAl, Inconel 718, X2CrNiMo18-14-3, and another austenitic steel at 684.5 nm," Int. J. Thermophys. 30, 1300-1309 (2008).
- 34 J. N. Hancock, T. McKnew, Z. Schlesinger, J. L. Sarrao, and Z. Fisk, "Infrared dynamics of YbIn_{1-x}Ag_xCu₄: Kondo scaling, sum rules, and temperature dependence," Phys. Rev. B 73(12), 125119 (2006).
- 35W. M. Rohsenow, J. R. Hartnett, and Y. I. Cho, Handbook of Heat Transfer (McGraw-Hill, 1998).